Ultrasonically Powered and Controlled Microsystem for Dual-Wavelength Optogenetics with a Multi-Load Regulation Scheme

Rashidi, Amin; Zamani, Milad; Mondal, Tanmay; Hosseini, Seyedsina; Laursen, Kjeld; Corbet, Brian; Moradi, Farshad

DOI
10.1109/LSSC.2023.3239601

Publication date
2023

Document Version
Final published version

Published in
IEEE Solid-State Circuits Letters

Ultrasonically Powered and Controlled Microsystem for Dual-Wavelength Optogenetics With a Multiload Regulation Scheme

Amin Rashidi, *Member, IEEE*, Milad Zamani, *Member, IEEE*, Tanmay Mondal, Seyedsina Hosseini, Kjeld Laursen, Brian Corbet, and Farshad Moradi, *Senior Member, IEEE*

***Abstract*—This letter presents an ultrasonically powered dual-wavelength optogenetic device that targets simultaneous excitation and inhibition of neural activities, or in a broader sense, optical stimulation in two distinct wavelengths for targeting different populations of neurons. This can be applied to a variety of neurological disorders. The device features a load regulator circuit that shares the available power budget between two μLEDs in a power-efficient and controlled way suppressing the need for adaptive matching and overvoltage protection circuits. Furthermore, the regulator circuit is capable of detecting power burst availability on the device and generating a control signal, accordingly. For 5.25-mW acoustic power at the device's surface, the rectified voltage, and the total current load of the system are regulated to 2.79 V and 600 μA, respectively. The maximum chip and device efficiencies of 92.5% and 31.8% are measured, respectively. The total die area in 180-nm CMOS technology nose and the estimated system volume are 0.16 mm^2 and 0.572 mm^3, respectively.**

***Index Terms*—Aperture efficiency, dual-wavelength optogenetics, dust, load regulator, piezoelectric, ultrasonic power transfer.**

I. Introduction

The emerging technology for ultrasonically powered implantable devices (i.e., neural dusts) has broadened to a vast variety of applications with variable electrical loads from few microwatts (e.g., neural recording [1], [2], [3], temperature sensing [4], pressure sensing [5], etc.) to several milliwatts (electrical stimulation [6], optogenetics [7], [8], etc.). This wide range of applications leads to a highly variable electrical load for multifunctional dusts. However, variable load opens up new challenges. A constant/no matching circuit can result in the degradation of aperture efficiency. Furthermore, small loads can lead to overvoltage conditions that can damage active circuits. The former has been addressed in [9] with an adaptive matching circuit at the cost of higher complexity, and uplink communication for tuning the carrier frequency. The latter is addressed in [10] by an overvoltage regulator. In this letter, we address both of the aforementioned challenges using a novel circuit for regulating the total electrical load of the dust by adapting the driving current that goes through a μLED for biomedical applications (e.g., optogenetics, light-driven drug delivery, or photodynamic therapy) according to other variable sources. Furthermore, the proposed circuit offers more advantages at no- or low-extra cost, including the longevity management of the energy stored at the dust, demodulation of time-encoded downlink data, weighted control of two loads using one set of data, and overvoltage protection. The proposed system targets the new BIPOLES tandem [11], which can be used for excitation and inhibition of the neurons at the same time. However, this can be applied to other applications within optogenetics, photodynamic therapy, and so on, where there is a dominant load. In the next section, the system architecture and the circuit designs are explained. Section III is devoted to the system integration and the measurement results and Section IV concludes this letter.

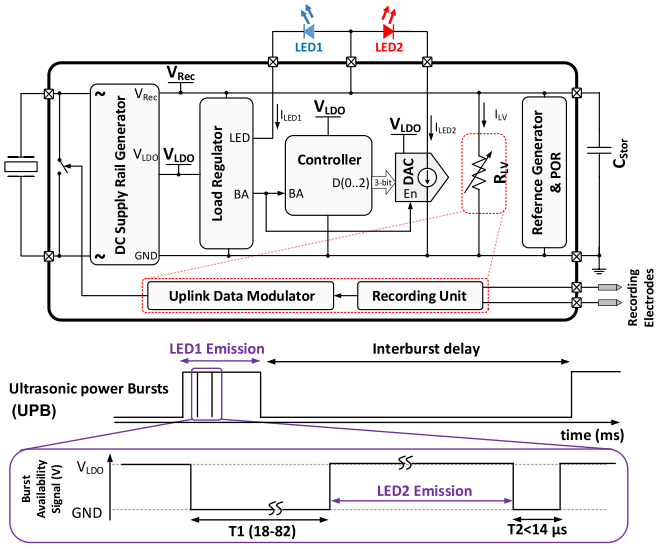

Fig. 1. Architecture of dual-wavelength optogenetic and its timing diagram.

II. Structure and Circuit Design

Fig. 1 illustrates the system-level architecture for the dual-wavelength optogenetic with the possibility of adding neural recording and backscattering circuits as other variable loads. The system includes a piezoelectric receiver, two μLEDs for dual-wavelengths optogenetics, an off-chip storage capacitor (C_{Store}), and a die for harvesting power and driving the μLEDs efficiently in a controlled weighted manner. The die includes a dc supply rail generator (including an active rectifier and a double-pass regulator), reference generator, and power on reset (POR) circuits adopted from [7]. Furthermore, the die features a novel load regulator driving a blue LED (LED1), and a controller followed by a current digital-to-analog converter (DAC) that drives the red LED (LED2) according to downlink data. The proposed load regulator is designed to adapt LED1 current (I_{LED1}) according to other current loads (I_{LED2} and I_{LV}) to regulate the total current load ($I_{\text{Total}} = I_{\text{LED1}} + I_{\text{LED2}} + I_{\text{LV}}$) to the desired value (e.g., which the simple matching circuit is designed for).

Manuscript received 9 November 2022; revised 6 January 2023; accepted 21 January 2023. Date of publication 25 January 2023; date of current version 9 February 2023. This work was supported by the Project STARDUST, which received funding from the European Union's Horizon 2020 Research and Innovation Program under Grant 767092. This article was approved by Associate Editor Ping-Hsuan Hsieh. *(Corresponding author: Milad Zamani.)*

Amin Rashidi is with the Faculty of Electrical Engineering, Mathematics, and Computer Science, Delft University of Technology, 2628 CD Delft, The Netherlands.

Milad Zamani, Kjeld Laursen, and Farshad Moradi are with the Department of Electrical and Computer Engineering, Aarhus University, 8000 Aarhus, Denmark (e-mail: mzamani@ece.au.dk).

Seyedsina Hosseini is with the Department of Health Technology Magnetic Resonance, Technical University of Denmark, 2800 Kgs. Lyngby, Denmark.

Tanmay Mondal and Brian Corbet are with the Tyndall National Institute, University College Cork, Cork, T12 YN60 Ireland.

Digital Object Identifier 10.1109/LSSC.2023.3239601

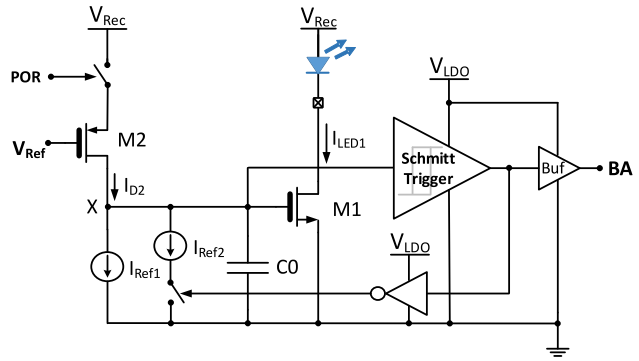

Fig. 2. Proposed load regulator schematic.

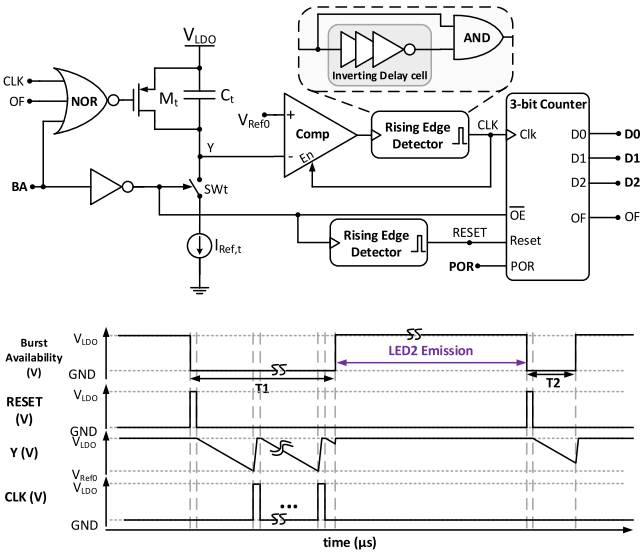

Fig. 3. Schematic of TDC and its timing diagram.

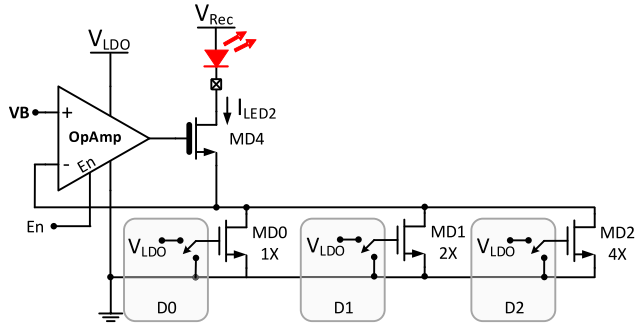

Fig. 4. Schematic of the current DAC block.

An external device generates a series of ultrasonic power bursts (UPBs) to drive the implant and send the optogenetic intensity data. As it is shown in the timing diagram of Fig. 1, the load regulator drives LED1 only upon the availability of the UPB. This helps in extending the longevity of the energy stored at the 100-nF C_{Stor} to be used by continuous low-power applications like neural recording circuits. However, LED2 is driven by the downlink command, embedded in the duration of predefined notches (T1 and T2) in the UPB.

The schematic of the load regulator is shown in Fig. 2. After receiving the POR signal (triggered when V_{Rec} rise above 2.2 V [7]), $M2$ senses the rectified voltage (V_{Rec}) as its source and gate are connected to V_{Rec} and V_{Ref} (1.46 V), respectively, and converts the voltage difference into current (voltage-to-current converter). As long as V_{Rec} is smaller than the target regulated voltage level (2.8 V), the drain current of $M2$ (I_{D2}) is smaller than I_{Ref1}, the voltage level at the gate of $M1$ (node X) is pulled down, and $M1$ is in the cut-off region. Upon receiving the UPB, as V_{Rec} is charged through the active rectifier and goes above the target regulated voltage, I_{D2} becomes dominant, the voltage level at node X (V_X) increases, and eventually, $M1$ turns on. However, increasing the current load, driven by $M1$ (I_{LED1}) results in a drop on the harvested dc voltage level and consequently I_{D2}. Thus, through a negative loop, the voltage level of V_{Rec} gets regulated. It happens for a certain I_{total} and available ultrasonic power at the dust. All in all, for a certain available power, $M1$ drives the LED1 with current level of $I_{\text{LED1}} = I_{\text{Total}} - I_{\text{LED2}} - I_{\text{LV}}$. Therefore, by setting I_{LED2} through downlink data, the proposed circuit divides the power/current budget between the two μLEDs in a power-efficient weighted manner while the total electrical load of the harvester stays constant. Since in the absence of UPB, V_X is pulled down by I_{Ref1}, a Schmitt trigger followed by a digital buffer digitizes V_X and shares it with other blocks as burst availability (BA) signal. Finally, in the absence of UPB (i.e., when M1 turns off), I_{Ref2} becomes parallel to I_{Ref1} for adding hysteresis to the circuit functionality and preventing undesirable ringings. The on-chip capacitor $C0$ is for ripple reduction at node X.

The schematic and the timing diagram of the controller block are depicted in Fig. 3. The circuit is mainly a time-to-digital converter (TDC), which is designed to control I_{LED2}. When the BA signal goes to zero (i.e., UPB absence), SWt closes a path, thereby the capacitor C_t is charged with a slope of $dv/dt = I_{\text{Ref},t}/C_t$, where $I_{\text{Ref},t}$ is a reference current. Then, a comparator followed by a rising ED circuit detects the time that voltage at node Y crosses the reference voltage, V_{Ref0}. An 80-ns pulse generated by the ED circuit at the node CLK triggers a 3-bit counter resets the charge over C_t and disables the comparator (to avoid a transition at its outputs as C_t discharges). Thus, the counter counts the number of CLK happening at time intervals of $t_{\text{LSB}} = (C_t/I_{\text{Ref},t})(V_{\text{LDO}} - V_{\text{Ref0}})$. Another ED circuit resets the counter on the onset of each notch. The counter releases the number, $D(0..2)$, when the notch ends and UPB is available again. During the notch, $D(0..2)$ are set to zero as the output enable (OE) of the counter is pulled down. If the counter counts more than 7, the counter sets its OverFlow (OF) output which keeps C_t in the reset state until the next notch, when the counter gets reset. Thus, during interburst delays, LED2 is off.

Fig. 4 illustrates the schematic of the employed current DAC. The DAC utilizes an opamp in negative feedback to set the drain voltage of the transistors MD0–MD2 to $V_B = 100$ mV. Thus, MD0–MD2 operate in the triode or cut-off region depending on the digital input. The drain current of MD0 in triode mode I_{D0} is equal to VB/R_{ON1}. The DAC generates 1-7 $\times$ I_{D0} by binary-weighted control of MD0–MD2 according to the downlink data. Here, I_{D0} is designed equal to 75 μA. The opamp gets disabled upon the unavailability of UPB, to help with the longevity of the energy stored on C_{stor}.

III. Measurement Results

Fig. 5 illustrates the die photograph of the purposed system. The whole die, including pads, measures 400 μ $\times$ 400 μm where the active area is 110 μm $\times$ 145 μm. Fig. 6 shows the schematic and a photograph of the experimental setup for transient measurements. A 2.55-ms burst signal with a carrier frequency of 2.79 MHz and including a series of notches with consequent durations of 20, 25, 33, 43, 53, 62, 72, and 4μs is fed to an arbitrary signal generator. The generated signal is amplified by a 50-dB power amplifier and transmitted as a UPB through a water tank and using a commercial

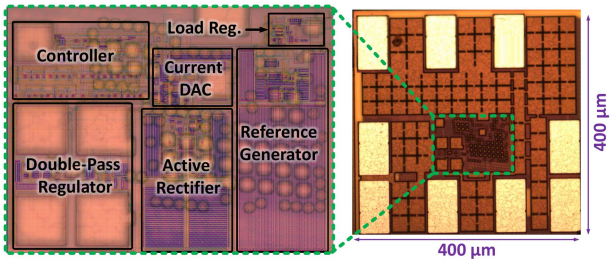

Fig. 5. Die photograph of the dual-wavelength optogenetic system.

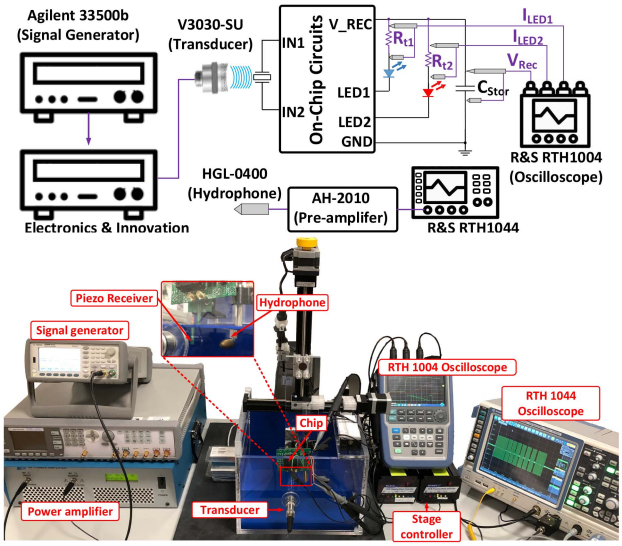

Fig. 6. Experimental setup for the transient measurement.

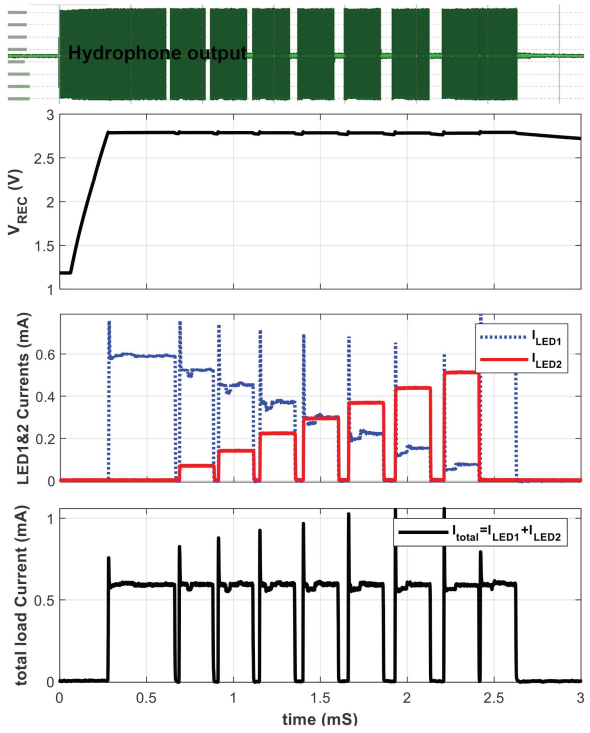

Fig. 7. Transient measurement results.

transducer. In the first step, the UPB is measured and validated by positioning a hydrophone in front of the transducer and capturing the UPB by an oscilloscope. In the next step, the prototype system

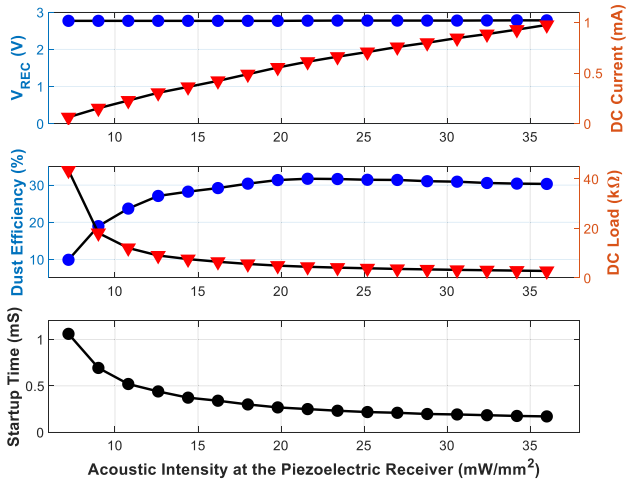

Fig. 8. (a) Rectified voltage and dc current load. (b) Dust efficiency and equivalent dc resistive load. (c) Startup time all over the acoustic intensity at the piezoelectric receiver.

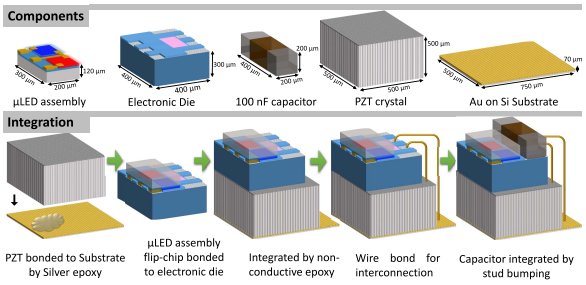

Fig. 9. Integration plan for the dust-sized system.

composed of a 500 μm × 500 μm × 500 μm piezoelectric receiver, the fabricated electronic die, the μLEDs, and the storage capacitors is moved in front of the transducer (i.e., in the same position that the hydrophone was placed in the previous step). Then, V_{REC}, I_{LED1}, and I_{LED2} are measured at the die's output using a hand-held oscilloscope at three of its isolated channels. The currents are obtained by measuring voltage over 50-Ω series test resistors (R_{t1} and R_{t2}). Fig. 7 presents the measured transient results at the output of the chip. As it is depicted in this figure, I_{LED2} increases from 0 to 514 μA with steps of 74 $\mu\mathrm{A} \pm 5\%$, V_{REC} is regulated to 2.8 V and $I_{\mathrm{Total}} = I_{\mathrm{LED1}} + I_{\mathrm{LED2}}$ is regulated to 600 μA. In another measurement, the ultrasonic intensity of 2.5-ms continuous bursts is swept from 7.2 to 36 mW/mm^2 with steps of 1.8 mW/mm^2. Accordingly, V_{REC}, the dc current (i.e., I_{LED1}), and startup times are measured. As illustrated in Fig. 8, the V_{REC} is measured 2.79 V $\pm$ 0.5%. However, as the acoustic intensity increases I_{LED1} increases and consequently the $R_{\mathrm{DC}} = V_{\mathrm{REC}}/I_{\mathrm{LED1}}$ decreases. In the middle plot of Fig. 8, the dust efficiency (output electrical power divided by acoustic power at the piezo surface) and R_{DC} are depicted, highlighting the dependence of aperture efficiency to the electrical load. Finally, in the bottom plot, the startup time of the chip is shown that decreases by increasing the acoustic power. An integration plan with estimated volume of 0.572 (1.3 × 0.80 × 0.55) mm^3, is shown in Fig. 9. In order to comply with this plan, the chip PADs have been designed in a way that the custom-made μLEDs and the capacitor can be mounted on top of the chip using flip-chip bonding, and stud bumping techniques, respectively. For dual μLED integration, first, the blue μLED is made on a sapphire substrate, then RED μLEDs are picked up from a releasable array and put beside the blue μLED using a

TABLE I
SUMMARY OF SPECIFICATIONS AND COMPARISON

	This Work	TBioCAS 2019 [7]	TBioCAS 2020 [8]	CICC 2018 [6]
Application	Dual-wavelength Optogenetics	Optogenetics	Optogenetics	Electrical stim.
Fully Programmable	Yes	No	No	Yes
Load Regulation	Yes	No	No	No
Technology	0.18 µm	0.18 µm	0.18 µm	65 nm LPCMOS
Chip Area/Active Area	0.17/0.016 mm2	0.09/0.0075 mm2	0.09/0.003 mm2	1/0.06 mm2
off-chip capacitors	100 nF	10 nF	10 nF	4 µF
Piezo/Dust volume	0.125/0.572* mm3	0.153 mm3/N/A	0.125/2.85 mm3	0.281/6.5 mm3
Carrier Frequency	1-5 MHz	1-7 MHz	1.38 MHz	1.85 MHz
Output power range	0.4-3 mW	2.28 mW	0-6 mW	3 mW
Max. VCR	94.5 %	93.57 %	90.4 %	N/A
Max. Chip efficiency	92.5 % @ 2.6 mW	94.51% @ 2.28 mW	91.2 % @ 2.4 mW	82% @ 120* µW
Overvoltage protection	Yes	No	No	N/A

* estimated

transfer printer. Then, interconnects are made using the metal evaporation process. A summary of specifications and comparison table is presented in Table I.

IV. CONCLUSION

This letter proposes a load regulation scheme suppressing the need for adaptive matching and overvoltage protection circuits for multifunction ultrasonically powered devices. It is shown that for the application of a dual-wavelength optogenetic system, the proposed circuit divides the power/current budget between the two μLEDs in a power-efficient weighted manner. Furthermore, the longevity of the energy stored at C_{Stor} is boosted by driving the μLEDs only upon the availability of UPB and disabling the unnecessary circuits in the absence of UPB. This way low-power circuits, such as neural recording, can be continuously powered by the stored energy at C_{Stor}.

REFERENCES

[1] D. Seo et al., "Wireless recording in the peripheral nervous system with ultrasonic neural dust," *Neuron*, vol. 91, no. 3, pp. 529–539, 2016.

[2] M. M. Ghanbari et al., "A $sub-mm^3$ ultrasonic free-floating implant for multi-mote neural recording," *IEEE J. Solid-State Circuits*, vol. 54, no. 11, pp. 3017–3030, Nov. 2019.

[3] M. Zamani, Y. Rezaeiyan, H. A. Huynh, M. Ronchini, H. Farkhani, and F. Moradi, "A 2.3-μW capacitively coupled chopper-stabilized neural amplifier with input impedance of 6.7 GΩ," *IEEE Solid-State Circuits Lett.*, vol. 4, pp. 133–136, 2021, doi: 10.1109/LSSC.2021.3094237.

[4] C. Shi, T. Costa, J. Elloian, Y. Zhang, and K. L. Shepard, "A $0.065-mm^3$ monolithically-integrated ultrasonic wireless sensing mote for real-time physiological temperature monitoring," *IEEE Trans. Biomed. Circuits Syst.*, vol. 14, no. 3, pp. 412–424, Jun. 2020.

[5] M. J. Weber, Y. Yoshihara, A. Sawaby, J. Charthad, T. C. Chang, and A. Arbabian, "A miniaturized single-transducer Implantable pressure sensor with time-multiplexed ultrasonic data and power links," *IEEE J. Solid-State Circuits*, vol. 53, no. 4, pp. 1089–1101, Apr. 2018.

[6] B. C. Johnson et al., "StimDust: A $6.5mm^3$, wireless ultrasonic peripheral nerve stimulator with % peak chip efficiency," in *Proc. IEEE Custom Integr. Circuits Conf. (CICC)*, 2018, pp. 1–4.

[7] A. Rashidi, K. Laursen, S. Hosseini, H.-A. Huynh, and F. Moradi, "An implantable ultrasonically powered system for optogenetic stimulation with power-efficient active rectifier and charge-reuse capability," *IEEE Trans. Biomed. Circuits Syst.*, vol. 13, no. 6, pp. 1362–1371, Dec. 2019.

[8] K. Laursen, A. Rashidi, S. Hosseini, T. Mondal, B. Corbett, and F. Moradi, "Ultrasonically powered compact implantable dust for optogenetics," *IEEE Trans. Biomed. Circuits Syst.*, vol. 14, no. 3, pp. 583–594, Jun. 2020.

[9] T. C. Chang et al., "Design of tunable ultrasonic receivers for efficient powering of Implantable medical devices with reconfigurable power loads," *IEEE Trans. Ultrason., Ferroelect., Freq. Control*, vol. 63, no. 10, pp. 1554–1562, Oct. 2016.

[10] A. Rashidi, K. Laursen, S. Hosseini, and F. Moradi, "Overvoltage protection circuits for ultrasonically powered Implantable microsystems," in *Proc. 41st Annu. Int. Conf. IEEE Eng. Med. Biology Soc. (EMBC)*, 2019, pp. 4354–4358.

[11] J. Vierock et al., "BiPOLES is an optogenetic tool developed for bidirectional dual-color control of neurons," *Nat. Commun.*, vol. 12, no. 1, p. 4527, Jul. 2021. [Online]. Available: https://doi.org/10.1038/s41467--021-24759--5